ELSEVIER

Thin Solid Films 418 (2002) 119–128

thin solid films

www.elsevier.com/locate/tsf

Characterisation of lanthanum lithium titanate thin films deposited by radio frequency sputtering on [100]-oriented MgO substrates

M. Morales[a,*], P. Laffez[a], D. Chateigner[b], I. Vickridge[c]

[a]*Laboratoire de Physique de l'Etat Condensé, Université du Maine, Avenue O. Messiaen, 72085 Le Mans Cedex, France*
[b]*Laboratoire de Cristallographie et Sciences des Matériaux (CRISMAT-ISMRA), 6 Boulevard Maréchal Juin 14050 Caen Cedex, France*
[c]*Groupe de Physique des Solides, Universités Paris VI et VII, 2 Place Jussieu, 75251 Paris Cedex 05, France*

Received 14 March 2002; received in revised form 19 June 2002; accepted 21 June 2002

Abstract

Highly textured and insulating $Li_zLa_{2/3\pm y}TiO_{3-\delta}$ ($\delta \leq 1$) thin films with structurally incorporated lithium, have been deposited for the first time onto MgO[100] substrates by radio frequency magnetron sputtering in an Ar/O_2 mixture. The chemical compositions of the films have been determined by Rutherford backscattering spectrometry and nuclear reaction analysis. The influence of the deposition conditions on the composition, the structure and the microstructure of the films have been analysed by X-ray diffraction, X-ray quantitative texture analysis and transmission electron microscopy, and their hetero-epitaxial growth modes are described.

Keywords: Oxides; Epitaxy; Sputtering; Insulators

1. Introduction

In the last few decades, considerable attention has been focused on rechargeable power sources as lithium ion batteries because of their high energy density and good cell performances, in which the choice of fast lithium ion conducting solids as electrolytes is crucial [1–5]. The lithium ion oxides $Li_{3x}La_{2/3-x}\square_{1/3-2x}TiO_3$ (LLTO), which crystallises in a perovskite derived structure [6,7], are very promising electrolyte materials due to their high ionic conductivity values at room temperature (approx. 10^{-3} S/cm for the composition $x \approx 0.11$) and an electrochemical window larger than 4 V [8,9]. The mechanisms of the ionic conductivity of the LLTO phase have been intensively investigated in the last years. Notably, the relatively higher ionic conductivity values reported in the literature for these phases have been correlated to the high mobility of the Li-ions through the vacant sites of the LLTO structure [10–13]. Then, their ionic conductivity has been evidenced anisotropic, and strongly correlated to the anisotropy of the structure, i.e. the distribution of the La ions in the double perovskite [14].

In the context of using films of the LLTO phases for the micro- and nano-technologies, operational miniaturisation of devices is needed. This implies a considerable research effort on micro-batteries used as power sources for smart cards or CMOS memories. Micro-batteries using LLTO compounds have already been elaborated in the form of sintered pellets with $LiCoO_2$ and $Li_4Ti_5O_{12}$ thin films as cathodes and anodes, respectively [15]. Such devices exhibit good performances (2 V developed voltage, stability with cycling, high current densities of 40 $\mu A/cm^2$, etc.) despite a high level of micro-structural defects and a large thickness (600 μm) of the LLTO electrolyte. Thin film technology allows the manufacturing of solid-state micro-batteries with thin electrolytes and large electrochemically active interfaces. Attempts to deposit $Li_zLa_{2/3+y}TiO_{3-\delta}$ thin films by laser ablation were shown recently to be very promising [16]. However, if this technique is appropriate

*Corresponding author. Tel.: +33-2-4383-3268; fax: +33-2-4383-3518.
E-mail address: magali.morales@univ-lemans.fr (M. Morales).

0040-6090/02/$ - see front matter
PII: S0040-6090(02)00624-7

Table 1
Cell parameters, composition and mean crystallite sizes of the studied thin films deduced from RBS, NRA, XRD and EDX analyses

	Deposition conditions		Cell parameters		$c/2a$	V (Å^3)	La/Ti (RBS)	La/Ti (EDX)	Li content z (NRA)	$Li_zLa_{2/3\pm y}TiO_{3-\delta}$	Mean crystallite size (Å)
	T (°C)	P_{O_2} (mbar)	a (Å)	c (Å)							
A	650	7.3×10^{-2}	3.91 (4)	7.90 (4)	1.010	120.776	0.83 (2)	0.89 (3)	0.02 (1)	$z=0.02$, $y^+\approx0.17$ (3)	236
B	700	7.8×10^{-3}	3.883 (7)	7.80 (3)	1.004	117.605	0.54 (2)	0.60 (3)	0.98[a] (1)	$z\leq0.46$, $y^-\approx0.13$ (3)[a]	271
C	700	7.3×10^{-2}	3.885 (2)	7.817 (2)	1.006	117.996	0.74 (6)	0.70 (7)	1[a] (1)	$z\leq0.24$, $y^+\approx0.04$ (7)[a]	511
D	750	7.3×10^{-2}	3.89 (2)	7.856 (9)	≈1.01	118.878	0.88 (6)	0.86 (7)	0.10 (1)	$z=0.10$, $y^+\approx0.21$ (7)	559
E	800	7.3×10^{-2}	3.889 (3)	7.888 (2)	1.014	119.300	0.72 (2)	0.75 (2)	0.02 (1)	$z=0.02$, $y^+\approx0.05$ (2)	682

[a] As all the XRD patterns have been indexed in a tetragonal cell in agreement with TEM and QTA analyses and as a pure LLTO solid solution is obtained for the compositional range $0.04<x<0.5$ according to the literature, a Li-rich impurity not visible in the XRD patterns must be present in the $Li_zLa_{2/3\pm y}TiO_{3-\delta}$ films.

The $-$ and $+$ exponents of y correspond, respectively, to the compositions $Li_zLa_{2/3-y}TiO_{3-\delta}$ (LLTO) and $Li_zLa_{2/3+y}TiO_{3-\delta}$. Numbers in parentheses represent errors on the last digit.

for fundamental purposes, its use on an industrial scale is still under progress for such materials. This led us to deposit LLTO thin films by radio frequency sputtering, a well-established technique in industrial processing. For the first time, we show in this work that the stabilisation of the $Li_zLa_{2/3\pm y}TiO_{3-\delta}$ [6,17] thin films can be achieved using single target deposition process. Temperature, oxygen pressure and the nature of the substrate should strongly influence the film structure and composition. Thus, we try to optimise the deposition conditions in order to obtain thin films with structural parameters leading to the highest conductivity values. Films were grown on polycrystalline platinum, Si[100] and MgO[100] single crystals. The crystallinity, texture, composition and microstructure of these films have been determined by X-ray diffraction, transmission electron microscopy and nuclear analyses, and the influence of the deposition conditions on these properties is discussed.

2. Experimental

LLTO targets of composition $x\approx0.11$ corresponding to the highest bulk ionic conductivity were synthesised by classical solid-state reaction according to the process reported in Fourquet et al. [6]. Stoichiometric mixtures of Li_2CO_3, La_2O_3, TiO_2 heated in air at 800 °C for 4 h were fired at 1150 °C for 12 h. The resulting powders were then pressed into pellets and sintered again twice in air at 1150 °C for 12 h.

Thin films were sputtered on polycrystalline platinum and Si[100] and MgO[100] single crystal substrates (5×10 mm). Reactive sputtering was carried out in a mixture of argon and oxygen atmosphere. The oxygen partial pressure, P_{O_2}, was varied between 9.6×10^{-4} and 7.3×10^{-2} mbar and the substrate temperature, T, was adjusted between 25 and 800 °C in order to determine the optimal deposition conditions. The sputtering conditions were the following: power density 7 W/cm^2 at 13.56 MHz and target–substrate distance of 40 mm. After sputtering, the thin films were kept for 1 h at their growing temperature and oxygen pressure. Then heating system and oxygen flux were turned off and the films cooled down. Five representative films (≈3000 Å thick) grown by varying the deposition conditions described in Table 1 were chosen for this paper.

Both initial targets and thin films have been characterised by X-ray diffraction (XRD) in the Bragg–Brentano geometry using CuKα radiation (X-Pert Philips diffractometer). The diagrams were recorded over the angular range $10°<2\theta<80°$ with a step of 0.02°.

As the XRD patterns of the corresponding thin films exhibited preferential orientations, X-ray quantitative texture analysis (QTA) was performed on these films. We used a Huber 4-circles diffractometer and the INEL curved position sensitive detector, which spans a 120° range in 2θ, allowing the simultaneous acquisition of several pole figures [18]. Pole figures were measured by scanning the tilt angle of the goniometer, χ, in the range 0–60° and the azimuthal angle, φ, in the range 0–360°, both using a 5° step. The integrated intensities are treated and corrected for absorption, volume variations and delocalisation effects [19]. In the direct integration approach of peaks that we are using, the defocusing effect is automatically corrected [20]. Pole figures are normalised into distribution densities that are expressed as multiples of a random distribution (m.r.d.). From several of these pole figures, we refined the orientation distribution function (ODF) using the WIMV method [21]. The ODF allows then the recalculation of the experimental pole figures and the completion of the blind and non-measured zones (appearing in white on the experimental pole figures). The calculation of the low Miller-indices pole figures allows simpler texture visualisation. All data reduction and calculations were operated using the Goman, Pofint [22] and Beartex [23] packages.

The composition of the sputtered films onto MgO substrates was determined by Nuclear Reaction Analysis (NRA) and Rutherford Backscattering Spectrometry (RBS) at the Van de Graaff accelerator of the Groupe de Physique des Solides, Jussieu (University of Paris VI, France). RBS Spectra were acquired with a 2 MeV incident beam of ^{4}He ions for 5 μC of incident charge. The detector was placed at 165°, and the solid angle was determined using a Bi-implanted silicon reference sample. Clear signals from Ti and La are obtained, allowing absolute determination of atomic area densities of these two elements and in addition, the ratio of La and Ti is obtained directly from the peak areas and the Rutherford cross-section, without need of reference. Since the films are deposited on an oxygen-containing substrate, it is not possible to use NRA to determine the oxygen content. However, an approximate idea can be obtained from the RBS spectra. We fitted these spectra using the RUMP simulation program [24] and varied the assumed oxygen composition to obtain the best fit. This is not very accurate, since the stopping power of the film may be different from that used in RUMP, calculated from the semi-empirical Ziegle–Biersack–Littmarck elemental values and Bragg's rule [24]. We estimate that the oxygen content of the film is determined to within approximately 30% using this method. Further measurements in progress are necessary before a more precise comment can be made on this point.

The lithium content of the films was determined using a 1 MeV incident beam of protons to induce the ^{7}Li(p, α) nuclear reaction, which has a cross-section varying slowly with energy in this range. The alpha particles were detected with a 300 mm^2 detector placed at 150°, which was protected from elastically scattered protons by a 19 μm Mylar film. Lithium area density was determined by comparison of peak areas with that obtained from a 15 μg/cm^2 LiF reference film on Mylar backing obtained from MicroMatter Inc. At the low beam current densities employed of 20 nA/mm^2 for the films and 2 nA/mm^2 for the reference, we confirmed that the alpha particle yields were stable up to three times the incident dose used.

Specimens for Transmission Electron Microscopy (TEM) observations were prepared by scraping off the thin films in ethanol using a diamond knife. A drop of the suspension was deposited and dried onto a carbon coated copper grid. TEM study of the scraped samples was performed in a 200 kV side entry JEOL 2010 Transmission Electron Microscope (tilt ±30°). Conventional bright field images and selected area electron diffraction (SAED) were used for the microstructure study. For comparison with RBS results, the La and Ti contents of the deposited material were determined by Energy Dispersive X-ray analysis (EDX) using a KEVEX and a LINK EDX Spectrometer coupled with a SEM Hitachi microscope and the 200 kV TEM microscope.

3. Results and discussion

3.1. X-Ray diffraction

The LLTO bulk compounds have been assumed to have in the compositional range $0.04 < x < 0.167$ a tetragonal structure (P4/mmm) derived from a perovskite-type structure ABO_3 [6]. Complementary studies have pointed out in these compounds the existence of a phase transition from tetragonal to orthorhombic (Pmmm) when the Li content decreased below $x = 0.06$, but with a weak orthorhombic distortion [7]. Recent neutron diffraction studies performed on the LLTO compound with the highest Li-substitution level, $Li_{0.5}La_{0.5}TiO_3$, have revealed that firstly this compound have a rhombohedral perovskite structure (R3c) with Li-ions not located at the A-sites of the perovskite as suggested previously [6], and secondly that the LLTO solid solution does extend up to values of $x = 0.167$ [10].

A typical XRD pattern of the LLTO targets is shown in Fig. 1a. A pure phase was found having the LLTO tetragonal structure [6] (space group P4/mmm) with unit cell parameters refined using the MAUD program [25] and deriving from that of the ABO_3 perovskite: $a = a_p = 3.874(3)$ Å and $c = 7.746(2)$ Å $\approx 2a_p$.

The stabilisation of the LLTO phase was only observed for thin films grown onto MgO[100] substrates (cubic system with $a = 4.21$ Å). Whatever the deposition conditions, the obtained films are transparent and insulators ($R \approx 10^{12}$ Ω) in contrast to those observed for thin films grown by laser ablation where $Li_zLa_{2/3+y}TiO_3$ insulator films are obtained only for oxygen pressures $P_{O_2} > 0.05$ mbar [16]. The oxygen pressure and the substrate temperature have an important effect on the crystallinity of the grown thin films and on their resulting X-ray patterns.

Fig. 1b shows the typical diffraction pattern measured on films grown at temperature $T \leq 650$ °C whatever the partial oxygen pressure (illustrated as sample A) and on films deposited at $T \geq 700$ °C with $P_{O_2} = 9.6 \times 10^{-4}$ mbar. The corresponding θ-2θ XRD pattern of sample A exhibits diffraction lines that are not well crystallised. This XRD pattern can be indexed in an apparent cubic crystalline system. The asymmetry and the width of these diffraction lines can be related to composition variations in these films, with cell parameters a comprised between 3.89 and 4.07 Å, and/or to the poor crystallisation of the film. It is a hard task to dissociate between crystal structure symmetry, cell parameter dispersions and axis orientations in such pseudo-symmetric films. The exclusive presence of the (h00) lines in the XRD pattern suggests a texture for this film with the a-

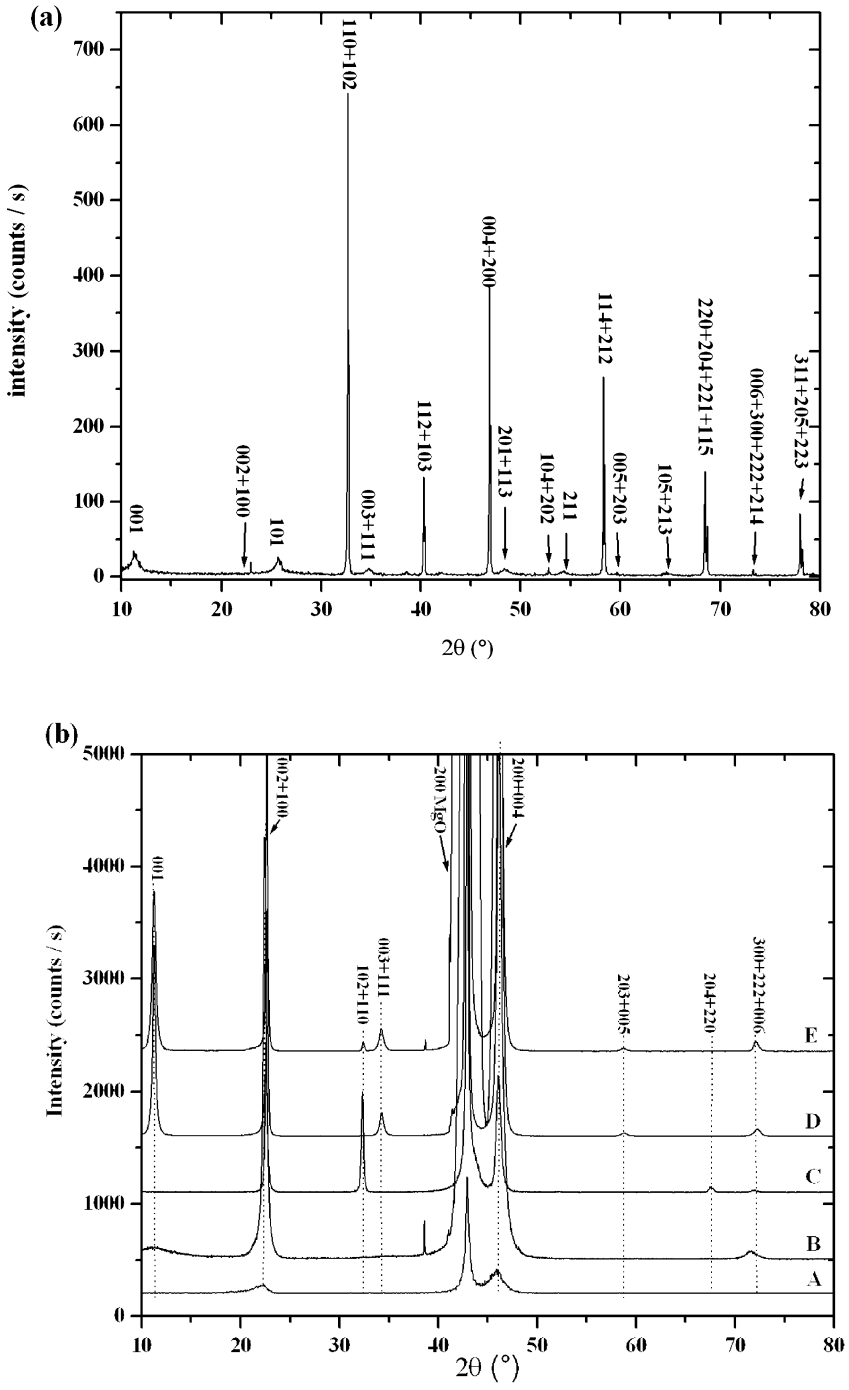

Fig. 1. XRD patterns of (a) the LLTO target and (b) the corresponding thin films synthesised for different temperatures and partial oxygen pressure showing preferential orientations. The small peak at $2\theta = 39°$ is only a $\lambda/2$ contribution from the substrate.

axis parallel to the normal of the film in a cubic system or an *a*-axis or *c*-axis orientation in a tetragonal system. In order to determine the averaged c/a ratio of this sample, we measured a χ-scan using an angular step of 1°, for the maximum of the 102 reflection of LLTO (tetragonal system). Since this line is located approximately 45° from the *a*- or *c*-axis, we operated this scan in the 40–50° range (Fig. 2). We clearly observe a shift of the contribution towards values higher than 45° and centred on 45.42° for the maximum of the dispersion. This is indicative of an average $c/2a$ ratio different from 1, and proves that the film is mainly tetragonal. Obviously, the width of the dispersion extends to more than 7°, including also the 45° position, and we cannot exclude completely the presence of a very minor cubic phase. Simple crystallography links the c/a ratio to the

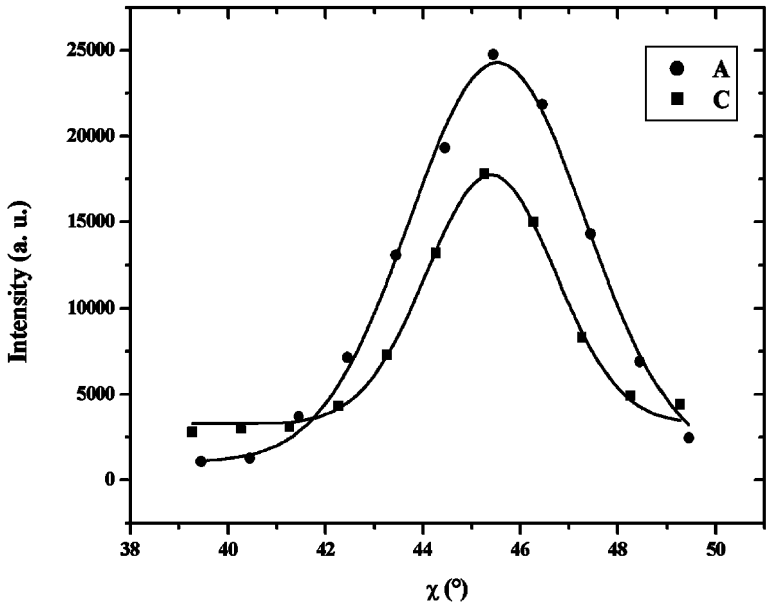

Fig. 2. χ-Scans of the {102} poles for samples A (circles) and sample C (squares), corrected from the delocalisation, and showing the tetragonal crystalline system of these samples. The same counting time has been used for both films. The interpolating lines are only guides for eyes.

observed χ angle of the dispersion. According to the literature [6,17], in the insulating $Li_zLa_{2/3\pm y}TiO_{3-\delta}$ systems we can suppose that generally $c>2a$ and then tan $\chi=c/2a$ for c-axis oriented parallel to the normal of the film plane, from which we obtain a $c/2a$ ratio of 1.01. The dispersion of the χ distribution can then be interpreted by a dispersion of c/a ratios, which is coherent with the extent of the Bragg peaks of Fig. 1b.

The diffraction patterns corresponding to the insulating films B, C, D and E grown at $T\geq 700$ °C and $P_{O_2}> 9.6\times10^{-4}$ mbar are shown in Fig. 1b. These XRD patterns exhibit only narrow peaks and are characteristic of fully crystallised films. They can all be indexed in a tetragonal structure in the P4/mmm space group. No evidence of impurities was observed in such patterns. Their corresponding cell parameters, determined using both classical XRD and texture data, are given in Table 1. The presence of the (00ℓ) reflections with ℓ odd in films B, D and E imposes the doubling of the c-axis of the LLTO phase [6]. These (00ℓ) reflections are not observed in the XRD pattern of sample C. This could be attributed either to a strong Li incorporation in the LLTO structure [6,7] or to a peculiar texture with no {00ℓ} planes parallel to the film plane. Fig. 1b shows that film C exhibits at least two texture components, with {102/110} and with {100/001} planes parallel to the film plane. But a quantitative texture analysis is required to check whether or not some {001} planes are aligned with the film plane or if the strong Li incorporation makes {00ℓ} planes with odd ℓs extinct [6,7]. Any cubic phase for LLTO in this film is excluded by its 102 χ-scan (Fig. 2), which is neatly centred on $\chi=45.23°$. Fig. 2 also shows the better crystallinity of sample C: the FWHM of the dispersion being approximately half that of sample A. The mean isotropic crystallite sizes of the thin films given in Table 1 have been estimated using the Laue–Scherrer formula. With the increase of the deposition temperature, and for a given temperature with an increase of the partial oxygen pressure, the crystallite size increases showing a better film crystallinity. The crystallite sizes do no extend over the whole film thickness. It can be linked either to some variation in compositions or to a local evolution of the texture (from the interface to the outer surface) and/or stresses in the films.

3.2. Quantitative texture analysis

Pole figures were measured and QTA operated on samples B, C and D. We observed the same texture for samples B and D, on which we concentrate now. The experimental and recalculated normalised pole figures of sample D are shown successively on Fig. 3a. A good reproduction of the experimental pole figures is obtained using the WIMV program. The average reliability factor of the refinement is of only $RP_1=57\%$ for the levels above 1 m.r.d. that attests for the quality of the ODF refinement for such strong textures. An estimate of the strength of this texture is given by the calculation of the so-called texture index [26] and of the texture entropy [27] which reach the values $F^2=209$ m.r.d.^{2} and $S=-2.6$, respectively. The texture index increases with the texture strength while the texture entropy (which measures the degree of disorder of the orientation) decreases

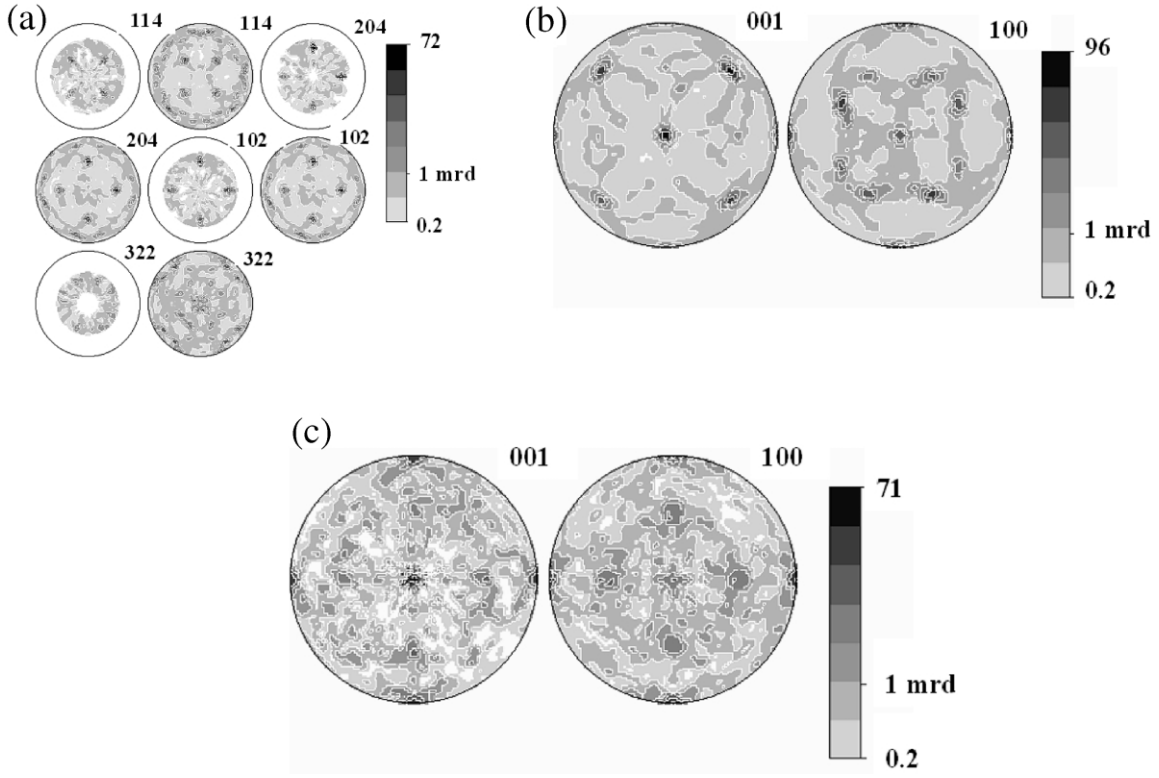

Fig. 3. (a) Experimental and recalculated normalised pole figures of sample D. (b) Recalculated low indices {001} and {100} pole figures for sample D. (c) Same for sample C. Values on the logarithmic scale bar are in m.r.d., equal area projections. Miller indices are shown for each pole figure. The minimum density levels have been fixed to 0.2 m.r.d. for clarity.

for strong textures. The F^2 values obtained in our films are larger than the ones obtained on simpler systems [28] and can be related in our films to a relatively low number of hetero-epitaxial relationships, synonymous of a higher crystallite organisation. Calculation of the low indices {001} and {100} pole figures allows a simpler texture visualisation (Fig. 3b). The {001} planes are preferentially aligned parallel to the film surface (pole figure plane), as seen by the strong pole in the centre of the {001} pole figure. This corresponds to a major texture component, with a maximum orientation density of 96 m.r.d. Two minor orientation components are visible, one with {001} planes perpendicular to the film surface (small reinforcements observed on the equator of the {001} pole figure) and the other with {111} planes parallel to the film surface (four poles located around $\chi = 70°$). For sample C, the orientation distribution function was refined with a reliability factor of $RP_1 = 33\%$. The calculation of the low indices {001} and {100} pole figures (Fig. 3c) shows three orientation components, the major one being the same as in samples D and B, but with a somehow lower texture strength ($F = 105$ m.r.d.^{2}, $S = -2.8$, maximum on the {001} pole figure, 71 m.r.d.). The {111} minor orientation component of sample D has been replaced by a component with {102} and {110} planes parallel to the film plane (four poles located at $\chi = 45°$ in the {001} and {100} pole figures, respectively) coherently with the diagrams of Fig. 1b. The reduction of the main component in this film compared to sample D is due to the relatively larger volume represented by the secondary components, in particular with {100} planes aligned with the film ({001} reinforcements on the equator are enhanced in sample C compared to D). Consequently, the non-observation of the {00ℓ} reflection in the θ-2θ XRD pattern of sample C must be attributed without ambiguity to a higher lithium content [6,7] incorporated in the LLTO film structure, than that incorporated in samples A, D and E.

3.3. Composition analysis

A typical RBS spectrum and its simulation are represented in Fig. 4. The La and Ti contents of the films deduced from RBS are given in Table 1 where they are compared to those determined by the EDX analysis. The RBS values are averaged over the film thicknesses, although the RBS spectra do show evidence of compositional variations as a function of depth. The La/Ti ratios are in good agreement with those determined by EDX (Table 1). For samples C and D, the RBS spectra

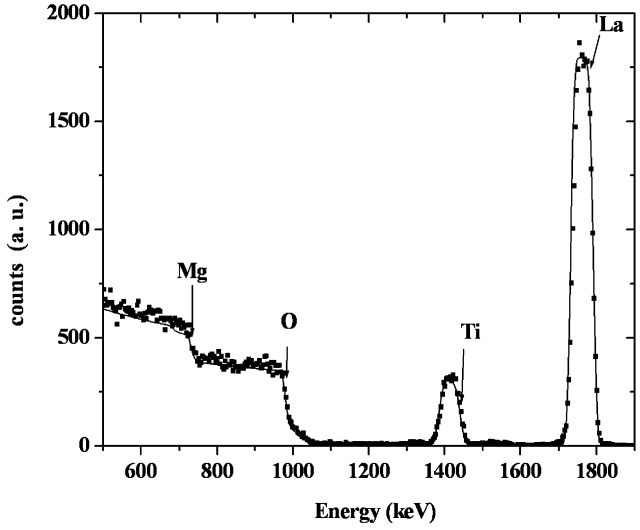

Fig. 4. Experimental Rutherford backscattering spectrum (square symbols) for sample A and its simulation (solid line) with the La/Ti ratio done in Table 1.

show clearly a diffusion of the lanthanum in the MgO substrate.

Whatever the deposition conditions, NRA shows that the Li ions are incorporated in the films (Table 1) in contrast to growth by laser ablation where the lithium is only incorporated for films grown for pressure $P_{O_2} > 5\times10^{-2}$ mbar [16]. We can give a composition $Li_zLa_{2/3\pm y}TiO_{3-\delta}$ of such film according to the literature [6,17] (with $2/3\pm y+z\leq 1$ if we consider that the Li ions are located on the A-site of the double-perovskite LLTO) and where δ is introduced to take into account the imprecision of the oxygen composition.

Since no impurity is visible from the diffraction patterns, the high Li content of films B and C ($z>0.5$, higher limit of the pure perovskite solid solution LLTO, see Fourquet et al. [6] and Kawai and Kuwano [29]) suggests either the presence of an amount of a Li-rich impurity (e.g. Li_2O) not visible in our XRD patterns or that the solid solution LLTO can extend up to values of $z=0.5$ as suggested in Alonso et al. [10]. For a given oxygen pressure ($P_{O_2}=7.3\times10^{-2}$ mbar), according to the variation of the intensity of the (00ℓ) reflections with odd ℓ indices, the Li content x increases dramatically between 650 and 700 °C. Then the Li content decreases due to the evaporation of the Li species when the substrate temperatures increase up to 800 °C. The refined a-cell parameters in the films are, respectively, approximately 3.88–3.91 Å as compared with the bulk materials LLTO ($a\approx3.874$ Å) [6] and $La_{2/3+x}TiO_{3-\delta}$ (3.88 Å $< a <$ 3.90 Å) [17]. The lower unit cell volumes determined by X-ray analyses correspond to the thin films grown at $T=700$ °C, namely B and C, which exhibit the higher lithium contents.

In thin films with composition $Li_zLa_{2/3+y}TiO_{3-\delta}$, the titanium cannot be fully oxidised to the +4 state [17]. However, as all the studied thin films are insulators, this suggests that the oxidation state of titanium, α, is in majority +4 ($\alpha\approx3.7$ according to Kim et al. [17]). From electro-neutrality rules for samples A and D, we find $\alpha\approx3.5$, and according to Kim et al. [17] and MacEachern et al. [30] a metallic behaviour would be expected in these films. As they are insulators and as the evolution of the unit cell volumes are mostly correlated to the largest ions La^{3+} content of the structure, this suggests that the number of La atoms incorporated in the $Li_zLa_{2/3+y}TiO_{3-\delta}$ phase is lower than those expected from Table 1. The La site occupancy in these films will be determined with a better accuracy using a new recent methodology for the analysis of X-ray diffraction data for highly textured thin films, the so-called combined analysis [25] that allows obtaining simultaneously reliable results of texture, structure and microstructural parameters, and will be described in a forthcoming paper.

3.4. Microstructural studies

Electron diffraction studies were performed in order to determine the microstructure of the studied thin films, which is closely related to their physical properties. Fig. 5 is a typical SAED pattern along the [100]* zone axis. It shows the single-phase nature of the selected area. Such pattern can be indexed in a first step using an apparent ideal cubic perovskite cell ($a\approx a_p\approx3.88$ Å). According to a previous study in the bulk LLTO materials [6], this pattern is more likely the superposition of two domains at 90°, with tetragonal cells $a\approx a_p$ and $c\approx2a_p$. No limiting reflections are evidenced which confirm the P4/mmm space group. The corresponding [100] HREM image (Fig. 6) exhibits domains oriented

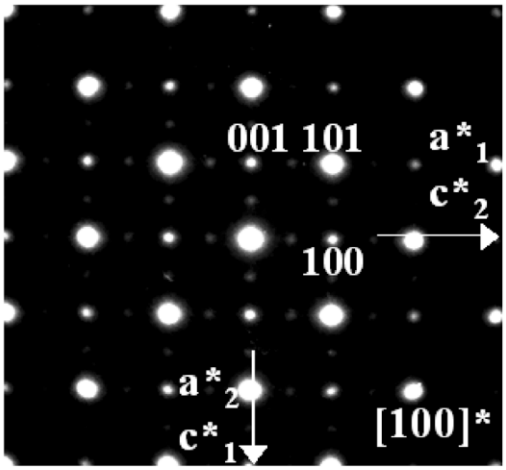

Fig. 5. Typical SAED pattern along the [100]* zone axis, indexed on the basis of the tetragonal LLTO cell.

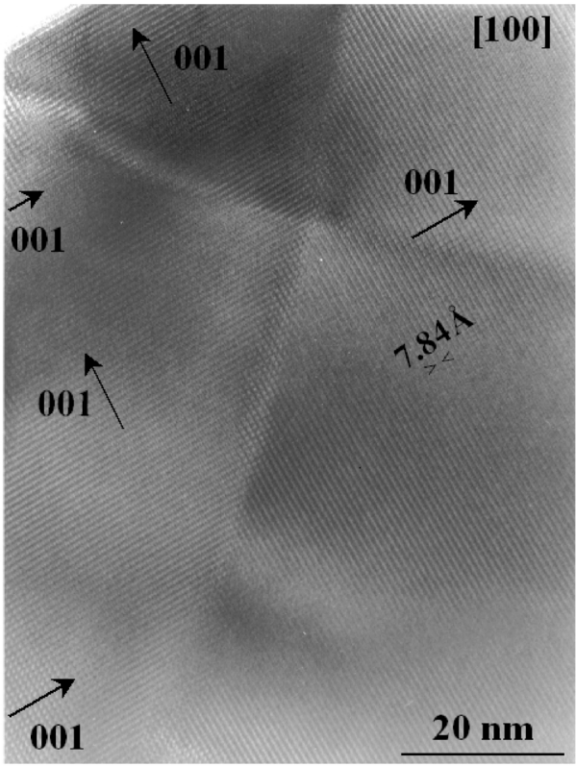

Fig. 6. ⟨100⟩ HREM image showing 90° oriented domains and their corresponding Fourier transforms that give the resultant diffraction pattern of Fig. 5.

at 90° with two possible orientations of the *c*-axis. The corresponding Fourier transform of these domains (insert of Fig. 6) confirms the two possible orientations of the *c*-axis and the periodicity along the *a*-axis. A coherent interface between theses domains along the $(110)_p$ directions is evidenced (Fig. 7). This microstructure with different orientations of the *c*-axis in the plane of the films is favoured by $c/2a$ ratios close to 1 (Table 1) and is consistent with the four-fold symmetry of the pole figures. In majority, all the obtained images (Fig. 7) show large domains with very few defects (dislocations, twinning, etc.) in general observed in perovskite thin films.

Fig. 8 shows a SAED pattern along the $[1\bar{1}0]$* zone axis evidenced for example in sample D and that confirms the doubling of the *c*-axis of the cubic perovskite cell, characteristic of the LLTO tetragonal cell. In this pattern, extra spots sometime appear at the position $(1/2, 1/2, \ell)$ with ℓ odd and suggest also a doubling of the unit cell along the diagonal of the perovskite, giving a local tetragonal $\sqrt{2}a_p \times \sqrt{2}a_p \times c \approx 2a_p$ unit cell yet proposed by Várez et al. [31] and called 'diagonal perovskite'. This SAED pattern can be explained by the superposition of two ED patterns indexed in two tetragonal cells: the LLTO cell and a body-centred (I) diag-

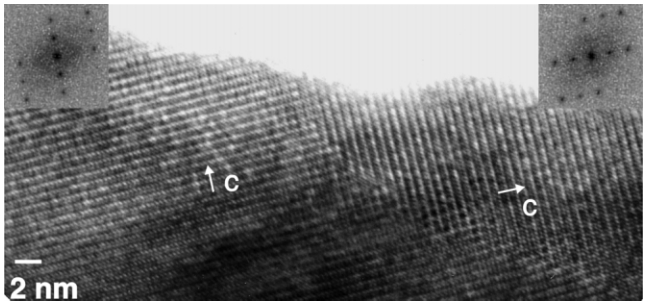

Fig. 7. ⟨100⟩ Low resolution image showing coherent interfaces between the domains along ⟨110⟩.

onal perovskite cell. In the corresponding $[1\bar{1}0]$ HREM image (Fig. 9), three areas labelled I, II and III were selected for Fourier transform. The corresponding Fourier transform patterns confirm the presence of small areas (areas I and II) with a local body-centred tetragonal diagonal perovskite unit cell (extra spot at the $(1/2, 1/2, \ell = 2n+1)$ positions). The presence of different ED patterns in our samples suggests local variations, minor in volume, in the ordering of the La and Li atoms [31,32]. Complementary detailed studies are in progress and will be reported elsewhere.

3.5. Growth schemes of LLTO on (100)-MgO

Electron microscopy and QTA results point out that the growth of LLTO films deposited on (100) oriented MgO single crystals is governed by hetero-epitaxial relationships. The main orientation component corresponds to the relation:

(001)-LLTO//(001)-MgO; [100]-LLTO//[100]-MgO

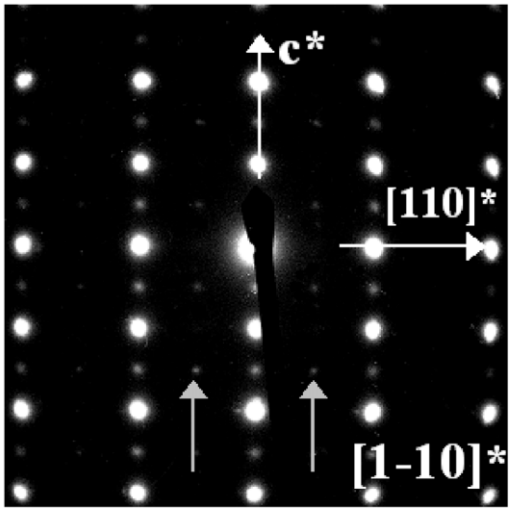

Fig. 8. SAED pattern of sample B along the $[\bar{1}10]$* zone axis indexed on the basis of the tetragonal LLTO cell. Grey arrows show extra $(1/2, 1/2, \ell = 2n+1)$ reflections that are sometimes observed.

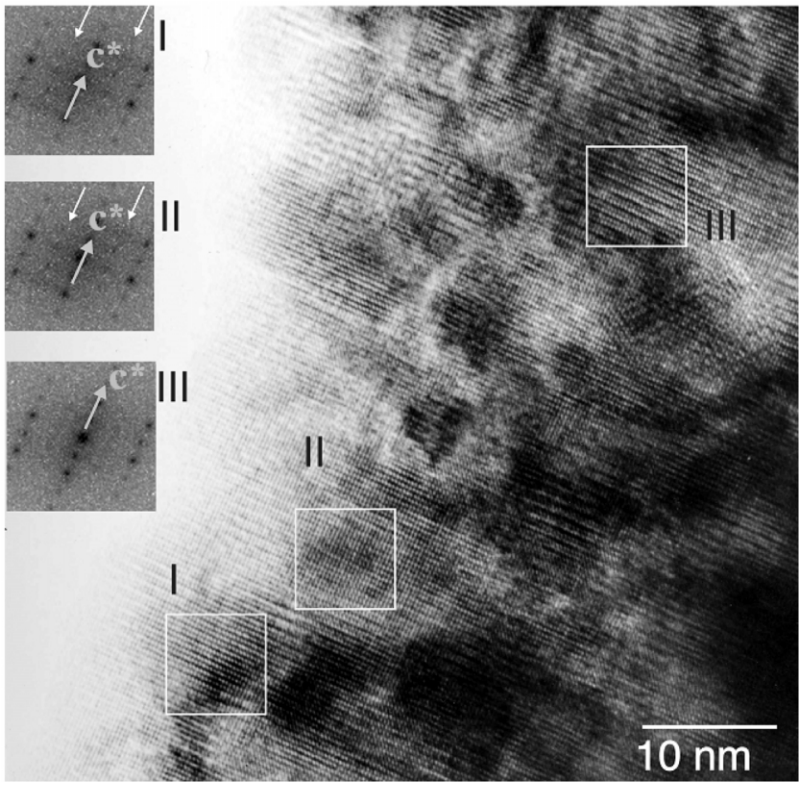

Fig. 9. $\langle\overline{1}10\rangle$ HREM image of sample B and Fourier transforms of different areas showing the combination (areas I and II) or not (area III) of the tetragonal LLTO cell and of the body-centred diagonal perovskite cell $\sqrt{2}a_p \times \sqrt{2}a_p \times 2a_p$.

This relation may be surprising since it corresponds to a lattice mismatch of approximately 8%. However, such orientations on MgO have been observed in similar perovskite systems such as high T_c superconductors and are explained by a continuous adaptation of the film cell through the thickness, via oxygen non-stoichiometry [33]. This could also be the case in LLTO films, though more investigation is necessary to establish it.

The minor texture components are stabilised with the hetero-epitaxial relationships:

(100)-LLTO//(001)-MgO; [100]-LLTO//[100]-MgO; [001]-LLTO//[010]-MgO

(102)-LLTO//(001)-MgO; [010]-LLTO//[100]-MgO, [10-2]*-LLTO//[010]-MgO

(111)-LLTO//(001)-MgO; [135]*-LLTO//[100]-MgO, [-1-35]*-LLTO//[010]-MgO

The first relation is realised with the same averaged mismatch as previously because of the pseudo-symmetry of the structure. The relative amounts of crystallites in the corresponding relationships will then be governed by the real c/a ratio of the film, and the temperature and oxygen pressure conditions during deposition. The two latter relations are accomplished with higher Miller indices and will consequently, correspond to the creation of larger interface energies from the coincidence site lattice theory point of view. It looks coherent to find them in a lesser degree in our system.

4. Conclusion

For the first time, we showed that highly textured $Li_zLa_{2/3\pm y}TiO_{3-\delta}$ insulating thin films with Li incorporated in the structure could be synthesised by reactive sputtering onto MgO[100] substrate. Several texture components are generally achieved, which depend on the composition of the films and their deposition conditions, the main texture component being always the simple axis relationship of hetero-epitaxy. Temperatures deposition at approximately 700 °C with oxygen partial pressure greater than 9.6×10^{-4} mbar lead to films with highest lithium contents and La/Ti ratios that give in the bulk LLTO materials the highest ionic conductivity values. These prototype depositions are very promising but as the aim of this work is to obtain thin films that can be used directly as electrolytes in micro-batteries, further depositions on conducting substrates (Ti, MgO/Pt, $Si/SiO_2/TiO_2/Pt$) are also in progress. This work

will be completed in a forthcoming paper with electrochemical measurements.

Acknowledgments

We want to thank O. Bonkhe, H. Duroy (Laboratoire des Fluorures, Le Mans, France) and T. Brousse (Ecole Polytechnique de Nantes, France) for helpful discussions.

References

[1] J.B. Bates, N.J. Dudney, G.R. Gruzalski, R.A. Zuhr, A. Choudhury, C.F. Luck, J.D. Robertson, J. Power Sources 43/44 (1993) 103.
[2] P. Fragnaud, D.M. Schleich, Sens. Actuat. A 51 (1995) 21.
[3] P. Birke, W.F. Chu, W. Weppner, Solid State Ionics 93 (1997) 1.
[4] P. Birke, W. Weppner, Electrochim. Acta 42 (1997) 3375.
[5] C.H. Chen, Ph.D. Thesis, Delft University of Technology, The Netherlands, 1998.
[6] J.L. Fourquet, H. Duroy, M.P. Crosnier-Lopez, J. Solid State Chem. 127 (1996) 283.
[7] J. Ibarra, A. Várez, C. León, J. Santamaría, L.M. Torrez-Martínez, J. Sanz, Solid State Ionics 134 (2000) 219.
[8] J. Emery, J.Y. Buzaré, O. Bohnke, J.L. Fourquet, Solid State Ionics 99 (1997) 41.
[9] Y. Harada, T. Ishigaki, H. Kawai, J. Kuwano, Solid State Ionics 108 (1998) 407.
[10] J.A. Alonso, J. Sanz, J. Santamaría, C. Léon, A. Várez, M.T. Fernandez-Díaz, Angew. Chem. Int. 39 (3) (2000) 619.
[11] A.K. Ivanov-Schitz, V.V. Kireev, N.G. Chaban, Solid State Ionics 136/137 (2000) 501.
[12] C.W. Ban, G.M. Choi, Solid State Ionics 140 (2001) 285.
[13] J. Emery, O. Bonhke, J.L. Fourquet, J.Y. Buzaré, P. Florian, D. Massiot, C.R. Acad. Sci. II-C 4 (2001) 845.
[14] Y. Inaguma, J. Yu, T. Katsumata, M. Itoh, J. Ceram. Soc. Jpn. 105 (1997) 548.
[15] T. Brousse, P. Fragnaud, R. Marchand, D.M. Schleich, O. Bonhke, K. West, J. Power Sources 68 (1997) 412.
[16] M. Morcrette, A. Gutiérrez-Llorente, A. Laurent, J. Perrière, P. Barboux, J.P. Boilot, O. Raymond, T. Brousse, Appl. Phys. A 67 (1998) 425.
[17] I.S. Kim, T. Nakamura, Y. Inaguma, M. Itoh, J. Solid State Chem. 113 (1994) 281.
[18] J. Ricote, D. Chateigner, L. Pardo, M. Alguero, J. Mendiola, M.L. Clazada, Ferroelectrics 241 (2000) 167.
[19] J.J. Heizmann, C. Laruelle, J. Appl. Crystallogr. 19 (1986) 467.
[20] J. Ricote, D. Chateigner, Bol. Soc. Española Céram. Vidrio 38 (1999) 587.
[21] S. Matthies, G.W. Vinel, Phys. Status Solidi B 112 (1982) K111.
[22] GOMAN, INEL France SA Licence 1997; POFINT, 'Pole figure interpretation', CNRS-INEL France SA Licence 2002.
[23] H.-R. Wenk, S. Matthies, J. Donavan, D. Chateigner, J. Appl. Crystallogr. 31 (1998) 262.
[24] L.R. Doolittle, Nucl. Instrum. Methods B 9 (1985) 344.
[25] L. Lutterotti, H.-R. Wenk, S. Matthies, in: J.A. Szpunar (Ed.), Textures of Materials, 2, NRC Research Press, Ottawa, 1999, pp. 1599–1604.
[26] H.-J. Bunge, C. Esling, in: H.-J. Bunge, C. Esling (Eds.), Quantitative Texture Analysis, DGM, Germany, 1982.
[27] S. Matthies, G.W. Vinel, K. Helming, Standard Distributions in Texture Analysis, 1,, Akademie-Verlag, Berlin, 1987, p. 449.
[28] D. Chateigner, B. Erler, Mater. Sci. Eng. B 45 (1997) 152.
[29] H. Kawai, J. Kuwano, J. Electrochem. Soc. 141 (1994) L78.
[30] M.J. MacEachern, H. Dabkowska, J.D. Garrett, G. Amow, W. Gong, G. Liu, J.E. Greedan, Chem. Mater. 6 (1994) 2092.
[31] A. Várez, F. García-Alvarado, E. Morá, M.A. Alario-Franco, J. Solid State Chem. 118 (1995) 78.
[32] H.-T. Chung, D.-S. Cheong, Solid State Ionics 120 (1999) 197.
[33] D. Chateigner, Ph.D. Thesis, Grenoble University, France, 1994.